Optical Neurostimulation Spine Endoprosthesis

Ricardo Morgado Marques
ricardo.m.marques@tecnico.ulisboa.pt

Instituto Superior Técnico, Universidade de Lisboa, Lisboa, Portugal

November 2019

Abstract

Optogenetic technologies offer an innovative and promising approach for addressing unmet clinical needs in the sphere of therapeutic and regenerative medicine. Although major breakthroughs have been made on this technology during the last decade to enable optogenetic control in normal and disease states using implantable devices, there is much potential for further improvements concerning these tools. This thesis focuses on the development of a biomedical spine endoprosthesis capable to delivering optimized optical stimulation to optogenetically targeted cells.

The neurostimulation endoprosthesis performs optical cell stimulation through LED channels and relies on programmable electronics to control light properties, such as wavelength, power density and pulse cycle. The purposed device is powered through inductive energy transfer and its wireless power transfer system was designed following an optimization process. Aiming to maximize its performance, it was possible to reach an efficiency value of 74.3% through a body tissue phantom. In order to observe cell response to blue illumination, *In vitro* experiments with miniSOG-targeted cells were conducted. These observations revealed that a light power density $3.33 mm/mW^2$ is sufficient to elevate the fluorescence level to its maximum value, which might imply its maximum capability of generating single oxygen. After testing a number of parametric model structures on the observed behaviour of a few cells upon blue illumination, a second order model suited the general miniSOG-targeted cell system satisfactorily.

The research and experiments performed in this work hold a "proof-of-concept" utility and serve as starting point for further development of the presented technologies.

Keywords: Optogenetics, Optical Neurostimulation, miniSOG, Therapeutic and Regenerative Medicine, Implantable device

1. Introduction

The peripheral nervous system (PNS) and spinal cord play a vital role in how information is communicated throughout the human body. The spinal cord is responsible for the connection between the brain and the PNS, which includes sensory receptors that help in processing and reacting to changes in the internal and external environment as well as to control muscles. Damage to the spinal cord and PNS resulting from trauma or disease often leads to debilitating neurological conditions which constitute an economical burden as well as personal and family suffering.

Optogenetics offers the possibility of optically controlling the activity of genetically specified cells [1], by combining light-sensitive proteins with controlled photo-stimulation. These proteins act as ion channels and pumps are genetically introduced into neurons, enabling the control of their activity on a millisecond time scale with high spatial resolution. Due to the opportunities this technology provides, this technology holds great potential for both studying the nervous system and providing innovative therapeutic and regenerative solutions for injured patients [2]. Despite the significant progress made in recent years, a great deal remains to be done. The integration of optogenetic technologies in living bodies paves the way for achieving the full potential of this technology by manipulating cell activity *in vivo* [3]. On the other hand, plenty of challenges emerge on the horizon. Cell photostimulation in a living body requires medical implantable devices to carry out effective high-precision light delivery. Simultaneously, supplying power to theses devices is also a critical factor determining their reliability. Optimal optical cell stimulation parameters are required so as to obtain precise responses and reduce losses.

2. Optogenetics in Neural Systems

2.1. Opsin Family of Optogenetic Actuators

Type I opsins are protein products of microbial opsin genes and are termed rhodopsins when bound to retinal. Neurons expressing opsins on their membrane surface enable optical neuronal modulation. When photo-activated, these

opsins function as gates for specific ions leading to either depolarization or hyperpolarization of cells. One class of microbial opsin genes encodes *halorhodopsins* (HR) which operate by pumping chloride ions from the extracellular to the intracellular space, resulting in hyperpolarization. After initial identification of halorhodopsin, other members of this class were also identified, such as *Natronomonas pharaonis*, which is sensible to yellow light (NpHR; [1]). On the other, in*channelrhodopsins*, another class of opsin genes, the ion-conducting activity is caused by the opening of a cation channel pore upon blue light, inducing cation flow that results in depolarization.

2.2. Therapeutic and Regenerative Advantages of Optogenetics

Optogenetic modulation of the neuronal activity is a major benefit for studying neuronal circuit dynamics which shape animal behaviour. More broadly, research on therapeutic methods is expected to benefit from optogenetic techniques. Functional electrical stimulation (FES) is the current clinical conventional approach used for neuronal stimulation to restore function and provide therapy in a wide range of clinical applications. However, these therapeutic approach bring up a few issues: i) electrical stimulation indiscriminately affects both neurons and fibers of passage, creating uncertainty regarding the predicted spatial effect of the method, ii) it is not possible o target specific cell types in the highly heterogeneous brain, and iii) the effects of electrical stimulation are often not clear as whether they cause excitation, inhibition, or both. On the other hand, optogenetics provides temporally precise, time-resolved to the millisecond timescale, control of activity in well-defined neuronal populations.

Additionally, optogenetics might play an important role in regenerative medicine. In case of spinal cord injury, astroglial cells, which play a critical role in neuronal survival and synaptic transmission, form a glial scar to close the wound and control the damage. However, reactive astroglia and the glial scar are strong physical and chemical barriers that inhibit neurogenesis and axonal outgrowth, preventing tissue regeneration later on[4]. Optogenetic may enable a fine control of astroglia to retain their protective role while promoting neurogenesis and CNS repair. The control of cell behaviour can be achieved by means of light-sensitive effector proteins, such as rhodopsins or the mini singlet oxygen generator (miniSOG) protein. MiniSOG is a relatively new fluorescent protein tag that can be used for disrupting cell function or killing specific cells.

2.3. Light Delivery

A key factor for achieving successful photostimulation is a practical and effective light delivery during neuronal activity modulation. Initially, solutions to this problem *in vivo* depended on tethered optical fiber-based systems, in which a fiber optic is inserted inside the brain of the animal subject to study [1]. However, these systems impose significant constraints on experimental design and interpretation of the results. For example, the subjects of study are physically restrained by an attachment which limits the environments in which optogenetic experiments can be performed. For this reason, wireless-powered and battery-powered head-mounted devices were introduced in *in vivo* experiments[5]. Nonetheless, these devices were relatively bulky, making their application on the spinal cord and PNS very unlikely. The concept of wireless and battery-less devices, which benefit from power transmission, is becoming more critical in the medical device field as batteries have slow recharging rate, limited charge/discharge cycles, and become a bio-hazard if toxic materials are leaked. Some reported implantable devices [5] take advantage of micro-LEDs inserted into the site of stimulation. Optical fibers are typically able to illuminate ventral structures from the fiber tip, whereas micro-LEDs, which can come in a wide range of sizes, have the advantage of complete customization, including the shape and size of the photostimulator. Also, these systems are substantially less costly. Because of the low power demands of micro-LEDs, radio frequency power harvesting systems make it possible for an optogenetic system to be partially or fully implantable at the site of stimulation. Montgomery et al. reported the development of the first fully internal device [6] for wireless optogenetic stimulation of brain, spinal cord, or peripheral nerve endings. It consists of a power receiving coil, a rectifier circuit, and a micro-LED. The implant is powered through an inductive link between coils, at an operating frequency of 1.5 GHz. Due to its shape and size, the new device was implanted in peripheral locations for stimulating targets beyond the brain.

2.4. Neuronal Activity Readouts

A fully equipped neuroscience optical toolbox should include multiple reliable readout technologies for answering a broad range of experimental questions, *in vitro* and *in vivo*. The three main categories of measuring methods are: electrical, optical, and magnetic resonance. Simultaneous optical stimulation and electrophysiological recording (patch clamping technique) of neuronal activity *in vivo* became possible with integrated submillimeter scale optical stimulators (such as fiber

optics) and recording electrodes [5]. Getting this feedback is of high importance not only for experimental reasons but also for eventually creating closed-loop systems, allowing therapeutic stimulation parameters to be rapidly set in patients. On the other hand Optical neuronal activity is appealing as it can provide spatial distribution and cell type-specific through changes in fluorescence levels. Voltage-sensitive dye (VSD) imaging is also an effective alternative for monitoring the electrical activity of large populations of neurons with high temporal resolution. Finally, optogenetic functional magnetic resonance imaging (ofMRI) is a technique which combines the spatial resolution of high-field fMRI (functional magnetic resonance imaging) with the high level of optogenetic stimulation precision, enabling cell type-specific mapping of functional neural circuits and their dynamics across the brain.

2.5. Optical Control Of Neural Activity

A fundamental goal in biology is to be able to control defined cells within functioning tissues. Temporal precision of control is important as cells may carry out different computations and deliver different outputs depending on the timing and context of the input signals. Optogenetic technologies transform brief pulses of light into precisely timed gain-of-function or loss-of-function of specified events in targeted cells [7]. Most published optogenetic experiments in behaving animals can be categorized as open loop systems. In these experiments, light stimulus parameters (such as pulse frequency and duration) are selected on the basis of previous literature or direct neural recording, without directly feeding back the measured neural effects of the stimulation online. In closed-loop optogenetics, the control action is a structured light stimulus that is automatically adjusted on the basis of the difference between desired and measured outputs, which may include electrophysiological, optical or behavioral readouts of activity generated by a biological system. Systems identification of optogenetic systems creates a connection between biological applications and the sphere of systems and control theory, similarly to what has been used effectively in the world of engineering for understanding and modulating complex dynamical systems.

2.6. Systems Identification for Neurons

Neuronal circuits, as neurons themselves, are very complex systems, which are not only nonlinear, non-stationary and different from each other but they also change dynamically, on millisecond timescales [7]. Online algorithms are necessary for designing light stimulation based on the observed neural behavior. Neuronal activity is measured by sensors which transfer the information to a controller, where it is used to build an estimation of the current state of the neural system. Algorithms use this estimation to compute a control action intended to achieve a desired activity level. This control action is carried out and the reaction of the system is, once more, recorded by the same sensors, closing the loop. Closed-loop control in optogenetics implicitly requires the existence of a model relating optical inputs to reactions on the neural system. For classical systems, this model is called "input transfer function".

Estimating the tween optogenetic stimulation and neuronal reaction of an individual or a group of cells of a is known as system identification. In a SISO (single-input-single-output) system, it is possible to effectively achieve "system identification" without directly modelling the system by using a PID controller. In "black box" modeling, a closed-loop control can be achieved by integrating through a parameter model aiming to fit a desired action. On the other hand, in "white box" modeling there is an accurate physical model of the system. In this case, black box modeling would consist in fitting the relationship between light inputs for optogenetic control and synchronous activity measurements. Limited system knowledge and imperfect control may lead to a "model-free" approach, like PID control system. Essentially, system identification should be considered both as a tool for understanding the system through reverse engineering. It also provides the basis that precede the control applications, like neural prosthetics.

3. Methodology
3.1. The Optical Endoprosthesis Concept
The purposed implantable medical device consists of three main sections which work together aiming to deliver controlled stimulation to the targeted cells (Figure 1). The first section involves the power harvesting and converting system which, as the name points out, is responsible for collecting energy and making it available to be converted into light. This section includes a receiver coil, whose only function is to extract electromagnetic energy. The AC power provided is converted into direct current, ready to feed the second section of the device - the light delivery system. This section responsibility lies in delivering energy to selected cells in the form of photons, by extending the direct current to a μLED implanted at the site of excitation. It also includes a power sensing system aiming to provide feedback on light proprieties (useful for an open-loop system without feedback from cell response) and a sensing system for the purpose of monitoring of cell response to stimulation (useful for a

closed-loop system). The feedback provided by the sensing systems is sent to a microcontroller, which works as the "brain" of the implantable device and computes the necessary control actions for achieving a desired state. Finally, communication must occur between the implantable device and an external unit, enabling monitoring and control of the device. The communication section contains an antenna which could, eventually, be shared for both communications and power transmission.

Additionally, an external unit is essential for the operation of the implantable device. This includes a power source (come type of battery or charged storage) aiming to supply energy to the endoprosthesis, a power transmitter coil, a DC/AC converter for creating alternating current at a selected frequency (enabling the wireless energy transfer through electromagnetic induction), an antenna for communications and a power management, critical in optimizing and conserve the use of power. Figure 1 shows the medical device concept in a block diagram.
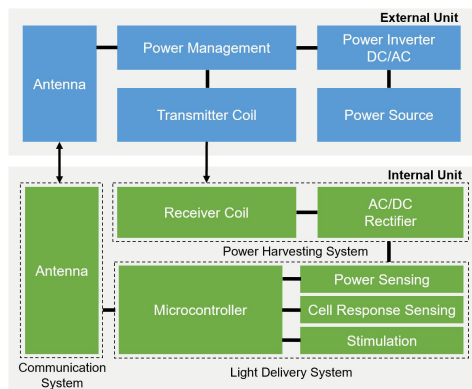

Figure 1: Implantable device and external unit.

3.2. Light Delivery System
3.2.1 Selection and Analysis of LEDs

Two types of LED were prepared to incorporate the endoprosthesis, to activate either NpHR or miniSOG-targeted cells, both valuable tools for therapeutic and regenerative ends. From the available literature, two important light requirements for optogenetic activation were collected: i) minimum the irradiance value of $5.4mW/mm^2$ for NpHR and for $0.5mW/mm^2$ miniSOG and ii) light wavelength of $589nm$ and $450nm$ respectively.

Two LED models were selected and analyzed regarding their wavelength and irradiance capabilities: LYT67F (max forward current of 50 mA) for NpHR and LD-MVSG (max forward current of 30 mA) for miniSOG. The measurement of the wavelength was obtained using a spectral color meter (UPRtek PG100N). The results (Figure 2) not only provide precise knowledge of the wavelength at a
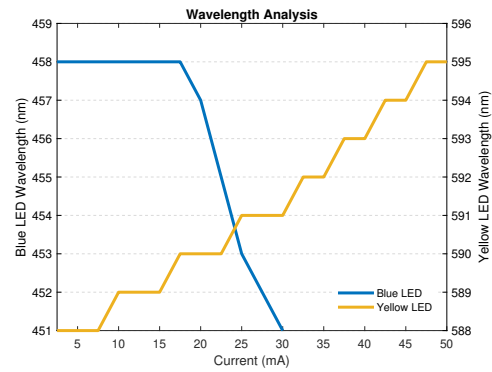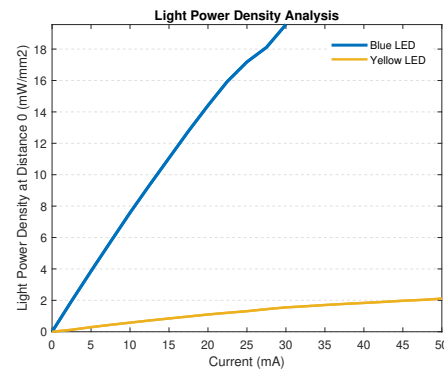

Figure 2: Wavelength proprieties analysis

Figure 3: Light power density proprieties analysis

certain current value, but they also establish an important interval of current values acceptable to work with during the biological experiments.

The light power of the LEDs was measured with a power meter (Thorlabs PM160). The values measured were divided by the LED emitting area to obtain the power density values. The results obtained were plotted against the current fed to the LED, as shown in Figure 3.

Although the blue LED selected (for miniSOG) has proven to meet the wavelength and the light power density specifications (spectrum band close to 450 nm and 2 mW/mm^2 respectively), the yellow LED (for NpHR) had a different outcome. Even though the light wavelength of the yellow LED fit the required value (spectrum band close to 589 nm), the irradiance values obtained are lower than the required ones, meaning that it does not deliver enough photons to activate the optogenetic tool.

3.2.2 Light Delivery Control System

Light proprieties can be regulated by actively controlling current supplied to the LED. Current value is therefore selected as the controlled variable. In order to create a closed-loop system, two elements were added to the system: i) a current sensor (INA219), responsible for creating a *feedback* and ii) a controller (*Arduino Uno*), in charge

of comparing it with the current state of the controlled variable and establishing a new adequate input. Due to the fact that *Arduino* uses "Pulse With Modulation" for creating analog outputs with digital means, a passive RC low pass filter was applied in order to transform the PWM into a constant stable signal, enabling adequate readings o current value by the INA219 sensor. The resistor and capacitance values are 3.3 Ω and 10 μF, respectively.

This control action is generated through a PI controller was programmed on the *Arduino*, which considers past and present values of the error. The gain values for the PI controller (loop tuning) were determined, aiming to achieve a responsive and stable loop with minimal overshoot. Initially, the Ki gain was set to zero. Then, Kp was slowly increased until the system reaches a point where the output current starts having high amplitude oscillation and eventually settles close the required setpoint and continues to oscillate at a reasonably slow pace between amplitudes close to each other. Secondly, the Ki value was increased until the setpoint is reached and reasonable time response was achieved. The Kp and Ki were set to 1.25 and 80, respectively. Finally, the dynamic behavior of the closed-loop system was tested both with different amplitude steps and pulse signals. The system has a rise time of 32 ms and a steady-state variance of 0.02.

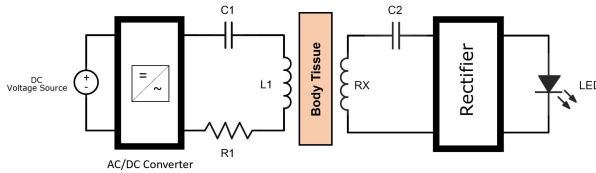## 3.3. Wireless Power Transfer System

Figure 4: Circuit model of 2-coil WPT system.

In implantable biomedical devices, the inductively coupled wireless power transfer scheme is preferred to transcutaneous wires due to a number of advantages, such as miniaturization, robustness, reliability of the operation and ease of implantation. Progressions in WPT designs are aimed to achieve maximum power transfer efficiency (PTE) through different layers for maintaining reliable operation of the implant. The WTP system uses a transmitter-receiver (Tx-Rx) coil pair for inductive coupling at a specific resonant frequency, with each coil being compensated by a capacitor to form a LC tank circuit with the same operating frequency. A schematic of a 2-coil WPT system is shown in Figure 4. C1 and C2 are the series resonant capacitors for the transmitting coil and receiving coil, respectively.

In order to reduce the risk of infection and im-prove the comfort of the patient, the size of the receiving coil should be minimized. Thus, the flat spiral-shaped coil type is selected as the coil type in this study, due to its compact shape. This enables the whole coil to be attached to the skin surface on both the exterior and the interior of the body. Additionally, a two-stage voltage doubling circuit using Schottky diodes (1N5817) was developed in order to convert alternating current into direct current at an operation frequency of 3 MHz. The first capacitor in series with the receiver coil (1.63×10^{-3} uF) was selected for being in resonance with the coil and other had a capacitance 10 uF.

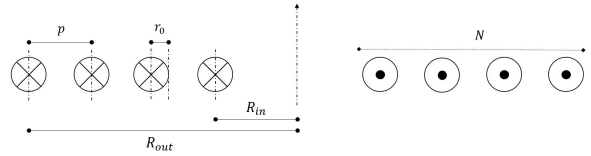### 3.3.1 Optimized Design of Coils

Figure 5: Design parameters of planar spiral coil (section view)

Figure 5 shows the geometry of the spiral shaped Tx and Rx coils. R_{out} is the outer radius, r_o is the wire radius p is the pitch, and N is the number of turns. The separation distance between Tx and Rx is defined by d. Coils are assumed to be perfectly aligned. Design constraints for the WPT system are shown in Table 1.

Parameter	Value (mm)
Rx outer radius, $R_{Rx_{out}}$	20
Tx maximum outer radius, , $R_{Tx_{out}max}$	30
Rx wire radius, r_{Rx_0}	0.25
Tx wire radius, r_{Tx_0}	0.25
Distance between Rx and Tx, d	10

Table 1: Rx and Tx coil geometry constraints.

Under resonant conditions, that is, when the driving frequency equals the resonant frequency ($f_d = f_r$), the power transfer efficiency (PTE) can be expressed a Equation 1:

$$PTE = \frac{R_L(\omega_r M)^2}{(R_2 + R_L)[R_1(R_2 + R_L) + (\omega_r M)^2]} \quad (1)$$

where M is the mutual inductance between coils, R_1 and R_2 are the primary and secondary circuits resistance, respectively and R_L is the load resistance. The self-inductance for flat, spiral coils is shown in equation 2.

$$L = \frac{N^2(2R_{out} - Np)^2}{162R_{out} + 28Np} \times \frac{39.37}{10^6} \quad (2)$$

For spiral coils at high operating frequencies, total resistance R_{AC} is originate from the proximity fac-

tor (R_{prox}) and skin effect (R_{AC}), as follows:

$$R_{AC} = l(R_{skin} + R_{prox}) \tag{3}$$

$$R_{skin} = R_{DC}(\frac{1}{4} + \frac{r_0}{2\delta} + \frac{3}{32}\frac{\delta}{r_0}) \tag{4}$$

$$R_{prox} = \frac{2}{\pi 2 r_0 \sqrt{1 - (2r_0/p)^2}} \sqrt{\pi \mu f \rho} \tag{5}$$

$$R_{DC} = \frac{1}{\sigma \pi r_0^2} \tag{6}$$

where l is the length of the wire used for the circular flat spiral coil, f is the operating frequency μ_0 is the permeability of free space, ρ is the resistivity and σ is the conductivity of the conductor, and r_0 is the radius of the wire, respectively. For perfectly aligned coils, mutual inductance can be calculated as follows:

$$m_{i,j} = \left(\frac{4R_{TXi}R_{RXj}}{(R_{TXi} + R_{RXj})^2 + d^2}\right)^{\frac{1}{2}} \tag{7}$$

$$G(m_{i,j}) = \left(\frac{2}{m_{i,j}} - m_{i,j}\right) K(m_{i,j}) - \frac{2}{m_{i,j}} E(m_{i,j}) \tag{8}$$

$$M_{i,j} = \mu_0 \sqrt{R_{TXi}R_{RXj}} G(m_{i,j}) \tag{9}$$

$$M = \sum_{i=1}^{N_{Tx}} \sum_{j=1}^{N_{Rx}} M_{i,j} \tag{10}$$

M_{ij} is the mutual inductance between i^{th} Tx loop with R_{txi} radius and j^{th} Rx loop with R_{rxj} radius. The distance between i^{th} and j^{th} loops is d (constant for all loops). Total number of turns in Tx and Rx coils are N_{tx} and N_{rx}. $K(m)$ and $E(m)$ are complete elliptic integrals of first and second order respectively.

Considering the constraints presented on Table 1, coil geometry is subject to an optimization process, aiming to achieve a maximum value of power transfer efficiency, as summarized the flow chart in Figure 6.
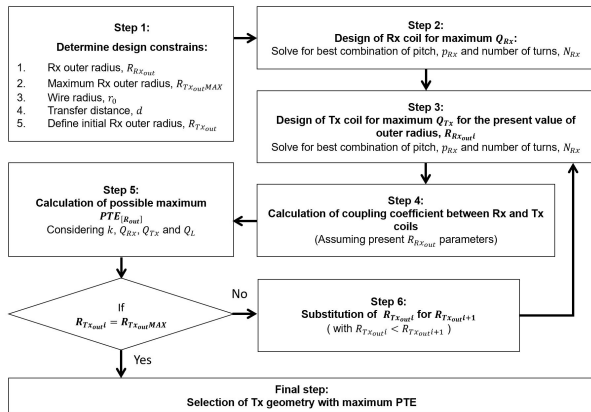

Figure 6: Design steps for purposed WTP system.

3.3.2 WPT System Validation

The circuit presented in Figure 7 was used to evaluated the WPT system performance. A sig-nal generator (SFG-1013) is used as a power supply to the primary circuit and the voltage across the load resistor is measured using an oscilloscope (TDS5034B). The plates holding the coils were set 10 mm apart. Following Equations 11 to 13, the PTE of the system can be obtained by measuring AC voltage U_in (V1), the voltage drop at the primary resistor, U_{R_1} and the voltage drop at a load resistance equal to 100Ω, U_L (V2), as shown in Figure 7. This process was repeated for various values of operating frequency with and without a body tissue phantom placed between coils.

$$PTE(\%) = \frac{U_L I_L}{U_{in} I_{in}} \tag{11}$$

$$I_L = \frac{U_L}{R_L} \tag{12}$$

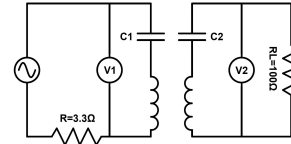$$I_{in} = \frac{U_{in}}{100\Omega} \tag{13}$$

Figure 7: Circuit used to evaluate performance of wireless power transfer system.

3.4. In Vitro Experiments
3.4.1 Transfection Procedure

In the present work, the transfection process was applied to HeLa cells using jetPRIME® reagent. The transfection followed the protocol recommended by manufactures (Figure **??**), with a ratio of $1\mu g$ of miniSOG plasmid per $3\mu L$ of jetPRIME® reagent and $300\mu L$ of jetPRIME® buffer. The mixture was added to HeLa cell cultures on $35mm$ glass-bottom dishes.

3.4.2 DMI6000B Light Power Density

In the *in vitro* experiments, a Leica DMI6000B microscope was employed. The intensity of excitation light is controllable through the *Leica LAS X* software, with 6 intensity values available: 0%, 10%, 17%, 33%, 55% and 100%. Using the optical power meter PM160 (as in section **??**), the excitation light power was measured and divided by the projected area on cell culture, obtaining the light power density of the excitation light. The irradiance values were equal to 0.46, 0.78, 1.74, 3.33, 5.99 mm/mW^2, following the same ascending order as in intensity value mentioned.

3.4.3 Imaging and Fluorescence Quantification

For fluorescence imaging of HeLa cells, a Leica DMI6000b widefield microscope with a HC

PLANAPO 10x, 0.4 NA objective with a X camera was used. Acquisition of images, and adjustment of their brightness and contrast, was performed using *Leica LAS X* software. For analysis and quantification of fluorescence, *Fiji* software was used. Cell grey value was divided by the nearby background grey value and the ratio was used to measure and compare fluorescence gradient values.

3.4.4 System Identification Models

The general polynomial model (Equation 14) provides varying levels of flexibility for modeling the dynamics and noise characteristics.

$$A(z^{-1})y(t) = \frac{B(z^{-1})}{F(z^{-1})}u(t - n_k) + \frac{C(z^{-1})}{D(z^{-1})}e(t) \qquad (14)$$

Where $u(n)$ and $y(n)$ are the input and output of the system, respectively, $e(n)$ is zero-mean white noise or the disturbance of the system and z^{-1} is a time-shit operator. By setting one or more of A(q), B(q), C(q) or D(q) polynomials equal to 1, it was possible to create different model structures. ARX, ARMAX, OE and BJ structures were analyzed.

3.4.5 Evaluation Criteria

We used three criteria for comparing the performance of the different structures and selecting the most adequate, before converting it to a transfer function: i) Akaike Information Criterion (AIC), ii) Bayesian Information Criterion (BIC) and iii) Minimum Description Length (MDL). These three metrics are defined by the following equations:

$$AIC = Nlog(V) + 2n_p \qquad (15)$$
$$BIC = Nlog(V) + log(N)n_p \qquad (16)$$
$$MDL = V\left(1 + \frac{log(N)n_p}{N}\right) \qquad (17)$$
$$V = \frac{1}{N}\sum_1^N \epsilon(t, \hat{\theta}_N)(\epsilon(t, \hat{\theta}_N))^T \qquad (18)$$

where V is the loss function, N is the number of values in the estimation data set, $\epsilon(t)$ is a vector of prediction errors, $\hat{\theta}_N$ represents the estimated parameters and n_p is the number of estimated parameters. Additionally, the fit value between an estimated model and the measured cell response is calculated as follows:

$$Fit(\%) = \left(1 - \frac{\| y - \hat{y} \|}{\| y - \bar{y} \|}\right) \times 100 \qquad (19)$$

where y is the measured output, $\hat{y}$ is the simulated or predicted model output and $\bar{y}$ is the mean of y.

4. Results & Discussion
4.1. WPT System Experimental Verification
Following the optimization process described in the flowchart of Figure 6), the coil system PTE

was maximized (Figure **??**). The resulting geometric sizes and design parameters for each coil are listed in Table 2. Experimental verification of the developed WPT system was conducted, as described in section 3.3.2. Figure 8 shows the simulated and experimentally measured power transfer efficiency of design presented in Table 2 with a separation distance between transmitter and receiver coils of 10 mm. It is shown that, at an operation frequency of 3 MHz, the estimated efficiency is 87.3% and 88.4% for the optimization model and *Simulink*, respectively, while the experimental value measured is 76.6% through air medium and 74.3% through tissue medium. As estimated, the power transfer efficiency of the system decreases as the operation frequency is reduced.

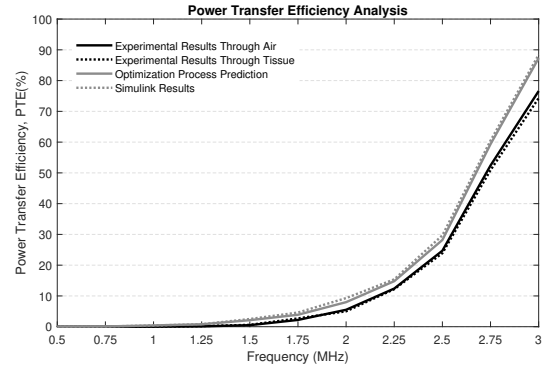| Parameter	Value
Tx outer radius, $R_{Tx_{out}}$	30 mm
Tx number of turns, , N_{Tx}	13
Rx number of turns, , N_{Rx}	9
Tx pitch, p_{Tx}	1.8 mm
Rx pitch, p_{Rx}	1.8 mm
Tx compensation capacitor, C_{Tx}	0.43 nF
Rx compensation capacitor, C_{Rx}	1.63 nF

Table 2: WPT system geometry

Figure 8: Power transfer efficiency values at different operation frequencies.

From Figure 8, it is clear that the use of capacitors for compensation, which create resonant conditions, enhances the efficiency of the transfer system. Furthermore, experimental measurements with body tissue phantom validated the effectiveness of the purposed wireless power transfer system when implanted. The evolution of discrepancy between efficiency levels of experiments through air and through the body tissue phantom along the frequency spectrum (Figure 9), demonstrates that the body tissue specific absorption rate (SAR) is proportional to the operating frequency, meaning an increase in losses that may result in temperature raise of surrounding body tissues.

4.2. Behavior Analysis of Living Cells
Initially, a cell culture area expressing a relatively high amount of transfected cells was irradi-
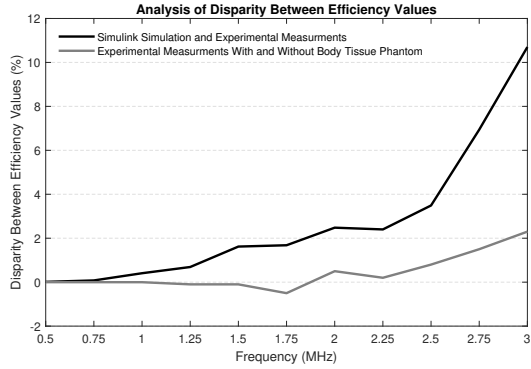
Figure 9: Discrepancy between power transfer efficiency results.

ated with each of the 6 available values of irradiance. Fluorescence images were captured and the change of fluorescence of number of cells was analyzed using *Fiji* software. Figure 10 shows the normalized fluorescence with respect to the maximum value for each of 8 randomly selected cells, in response to changes in the power density of blue light.
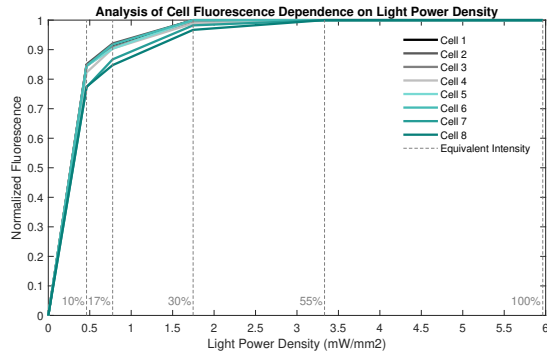

Figure 10: Normalized fluorescence of selected cells at different points of light power density.

The previously minimum reported light power density value used in experiments with miniSOG ($0.5mm/mm^2$) is shown to be enough to cause its activation, as all the observed cells react to the minimum irradiance available ($0.46mm/mm^2$) . The minimum light power density for causing 50% of maximum fluorescence is, therefore, under this value. Secondly, a light power density value between $1.75mm/mm^2$ and $3.3mm/mm^2$ seems enough to evoke the cell's full potential for generating singlet oxygen, as the fluorescence of all observed cells reaches its maximum level between these values (Leica DMI6000B do not allow intensity values between these two).

A second experiment was designed in order to capture the fluorescent behaviour of miniSOG-transfected cells upon an input of blue light. Cells were illuminated constantly with blue light ($6mW/mm^2$ at 450 nm) during a period of 5 min-

utes. Figure 11 shows the normalized fluorescent level throughout time with respect to the maximum value for each cell represented in Figure **??**, meaning that every cell starts with a fluorescence level of 1. In the systems identification context, this experiment would be equivalent to exposing a certain system (cell) to a step input (5 minutes illumination) of amplitude equal to $6mW/mm^2$. Image capture was processed in intervals of 10 seconds, resulting inn a sample time of the same value.
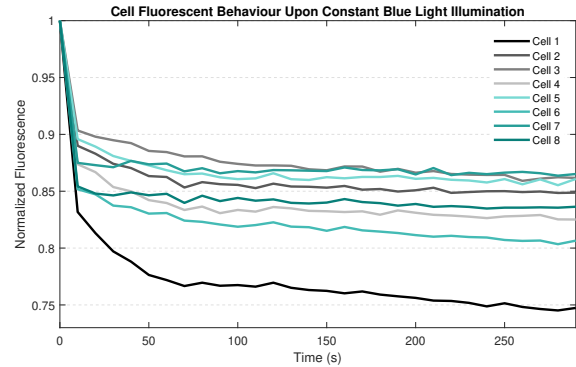

Figure 11: Normalized fluorescence of selected cells through time during experiment 2.

For the purpose of identifying a structure which would correctly model cell behaviour upon blue light, cell 3 was selected randomly among the observed cells. Then, using *Matlab*'s System Identification Toolbox as well as the cell response to the 5 minute step input ($6mW/mm^2$ blue light), shown in Figure 11, the various model structures (ARX, ARMAX, OE and BJ) were tested with various parameters and evaluated with the AIC, BIC and MDL metrics. These converged to the ARX(2,1,1), ARMAX(2,1,1,1), OE(2,1,1) and BJ(2,1,1,1) polynomial structures. After analyzing their stability by placing their zeros and poles on the z-plane, the OE and BJ structure were excluded for being non minimum phase system models, which fails to characterize fluorescence behaviour in the cell system.

An analysis of the response of the remaining ARX and ARMAX structures indicated very similar transient behaviour and steady-state error. Therefore, AIC, BIC, MDL and fit values for these two alternatives were compared and shown in Table 3.

	AIC	BIC	MDL	Fit
ARX	-375.04	-369.43	1.24×10^{-4}	92.44%
ARMAX	-367.59	-363.38	1.57×10^{-4}	93.03%

Table 3: Comparison of AIC, BIC, MDL and fit values for ARX and ARMAX models

Even though the ARMAX model presents a better fit value, the three metrics converge into the selection of the ARX alternative, as they all present values slightly lower for this model structure due

to its lower number of parameters. Further analysis with respect to the error between the output of these models and cell response were performed ($error = y - \hat{y}$), aiming at finding similarities between this error and white noise. Figure 12 indicates that autocorrelation of error is very similar in both models, with ARX model shown a bit more similarity to white noise (1 at 0 lag and 0 at the remaining lags). The mean value of the error ($E[error]$) for the ARX model is 1.53×10^{-4} and 1.72×10^{-4} for the ARMAX model, while, for white noise, this value is equal to 0. Because the ARX structure has less parameters and revealed a good performance on the evaluation processes, it is chosen to represent the cell system in further tests. Figure 13 compares cell 3 and ARX(2,1,1) model response to the step input of 5 minutes and show the percentage of error along time.
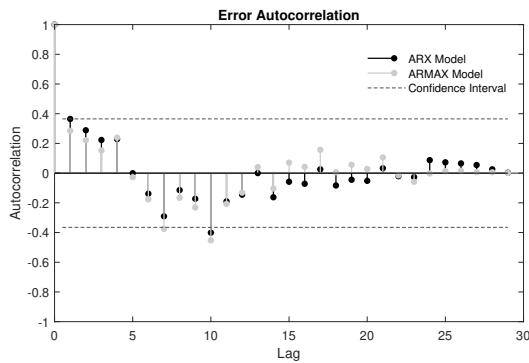

Figure 12: Error autocorrelation of error between the output of ARX and ARMAX models and cell response

ARX(2,1,1) models were tested in the remaining seven cells. Each cell response was compared to the respective ARX(2,1,1) model, and both model fit value and error autocorrelation were analyzed, respecting a similar process to the one followed with cell 3. Even though error autocorrelation exceeds the confidence interval in a few points in a few cells (particularly in cell 1), in general the results indicate that the tested model structure with one zero and two poles reproduces cell dynamics satisfactorily. Thus, considering the deterministic portion of the polynomial model, coupled to $u(t)$ in Equation 20, cell dynamics can be modelled with the following discrete transfer function:

$$sys(z^{-1}) = \frac{a_1 z^{-1}}{1 + b_1 z^{-1} + b_2 z^{-2}} \qquad (20)$$

where a_1, b_1 and b_2 parameters, which depend on each individual cell, are presented in Table 4.

In order to validate this model, data from a third experiment was employed. The same group of cells was subjected to a cycle of illumination involving 2 seconds of irradiance followed by 30 seconds of darkness during a period of 33 minutes. Image capture was processed during the the 2 seconds of illumination (exposure time), giving a sample time
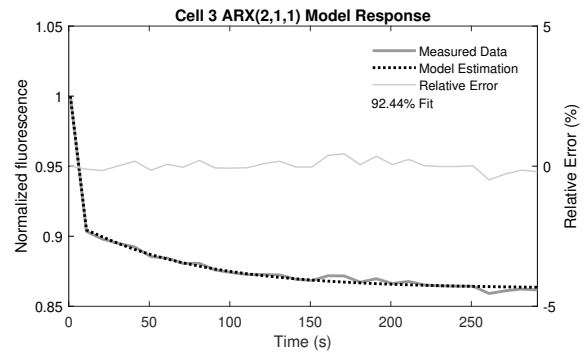

Figure 13: ARX(2,1,1) model comparison with cell 3 response.

	a_1	b_1	b_2
Cell 1	0.1626	-0.7951	-0.0109
Cell 2	0.2661	-0.6317	-0.0558
Cell 3	0.1135	-0.8630	-0.0555
Cell 4	0.2806	-0.5931	-0.0687
Cell 5	0.2969	-0.5934	-0.0623
Cell 6	0.1394	-0.8056	-0.0222
Cell 7	0.4303	-0.4854	-0.0188
Cell 8	0.2205	-0.7466	-0.0112

Table 4: ARX(2,1,1) model parameters for each cell.

of 30 seconds. Figure 14 shows the normalized fluorescent level throughout time with respect to the maximum value for each cell. In the systems identification context, this experiment would be equivalent to exposing a certain system (cell) to a square wave of 32 seconds period and a pulse width of 6.6%. The amplitude of this square wave was, as in experiment 2, equal to $6mW/mm^2$ at 450 nm.
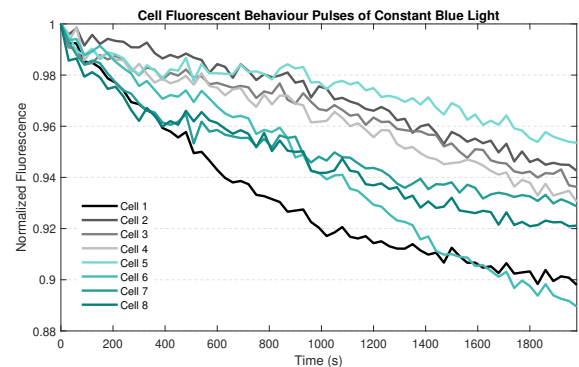

Figure 14: Normalized fluorescence of selected cells through time during experiment 3.

Firstly, cell 1 was selected randomly among the observed cells. Then, using *Simulink* Software, a square wave with similar proprieties to the one applied on the present experiment was used as input to a transfer function similar to the one on Equation 20 ($B(z^{-1})/A(z^{-1})$), with a sample time of 30 seconds. Likewise, a transfer function equal to $1/A(z^{-1})$ was used to characterize noise disturbances, as stated in the ARX structure. The parameters a_1, b_1 and b_2 of Equation 20 were modified until the output was sufficiently approximated to cell response in Figure 14. Figure 15 shows the
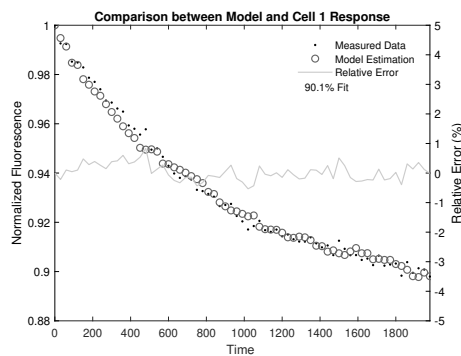
results of the validation process.

Figure 15: ARX(2,1,1) model response comparison with cell 1 response in experiment 3.

Figure 15 shows the results of the validation process. The ARX(2,1,1) model structure approximated satisfactorily the behavior of cell 3 in the second experiment, with a fit value of 90.1%. The same process was repeated for two other cells, chosen arbitrarily, and the results, shown in Figure **??**, were similar to those obtain with cell 1, with fit values of 80.6% and 76.6% for cells 7 and 8, respectively. Table 5 presents the parameters a_1, b_1 and b_2 for the three analyzed cells.

	a_1	b_1	b_2
Cell 1	0.0052	-0.5739	-0.3804
Cell 7	0.0041	-0.5639	-0.3804
Cell 8	0.0040	-0.5700	-0.3850

Table 5: ARX(2,1,1) model parameters for each cell.

Even though the fit values were slightly lower in the validation process ($\sim$10% lower), this might be a consequence of the system identification method, which involved an iterative process of adjusting the combination of the three parameters (a_1, b_1 and b_2), using only fit value as a figure of merit. After applying the system identification methods presented in this chapter, a deterministic model structure of two poles and one zero fairly describes the the miniSOG-targeted cell system.

5. Conclusion

The present work focused on the development of neurostimulation endoprosthesis involving optogenetic technologies. Two LED models available in the market were selected and analyzed regarding light proprieties for activation of both NpHR and miniSOG proteins. A light control system involving an *Arduino Uno* to control the current supplied to the LED and a current sensor (INA219) to provide feedback and close the loop were developed, using a proportional-integral (PI) approach for the blue LED, achieving a stable current value within a ±0.2 mA margin around the desired value .

An optimized wireless power supply system based on an inductive link between a pair of transceiver and receiver coils was developed as well as a two-stage voltage multiplier in order to rectify AC current. The resulting inductance coils were compensated by capacitors, creating resonant conditions which were demonstrated to enhance efficiency levels. The efficiency of this system was experimentally measured through air and through a material with similar characteristics of body tissues, showing a power transfer efficiency of 76.6% through air and 74.3% through body tissue phantom.

In vitro experiments using light properties similar to those of the blue LED model presented useful information on the behaviour of living miniSOG-targeted cells upon blue light activation. Experiments with different values of light intensity demonstrated that a power density value near $0.5mW/mm^2$ results in a fluorescence response of around 80% of the maximum fluorescence potential of the cell, which is achieved with values between $1.75mW/mm^2$ and $3.3mW/mm^2$. Additionally, a miniSOG-targeted cell culture was illuminated during 5 minutes at $6mW/mm^2$ in order to observe fluorescence decay and model cell response to light. After testing a number of parametric model structures and evaluation metrics, the ARX(2,1,1) and suited the general cell system satisfactorily. A third experiment and process of iteration between parameters values was used to validate this model structure. These experiments reveal a cell behaviour correspondent to a second order system with one zero and two poles.

References

[1] Ofer Yizhar, Lief E. Fenno, Thomas J. Davidson, Murtaza Mogri, and Karl Deisseroth. Optogenetics in Neural Systems, 7 2011.

[2] Kate L. Montgomery, Shrivats M. Iyer, Amelia J. Christensen, Karl Deisseroth, and Scott L. Delp. Beyond the brain: Optogenetic control in the spinal cord and peripheral nervous system, 2016.

[3] Rajas P. Kale, Abbas Z. Kouzani, Ken Walder, Michael Berk, Julian Berk, and Susannah J. Tye. Wireless Optogenetics: An Exploration of Portable Microdevices for Small Animal Photostimulation. *Procedia Technology*, 2015.

[4] R. Nieuwenhuys, J. (Johan) Voogd, and Chr. van. Huijzen. *The human central nervous system*. Springer, 2008.

[5] Rajas P Kale, Abbas Z Kouzani, Ken Walder, Michael Berk, and Susannah J Tye. Evolution of optogenetic microdevices. 2015.

[6] Kate L. Montgomery, Alexander J. Yeh, John S. Ho, Vivien Tsao, Shrivats Mohan Iyer, Logan Grosenick, and Emily A. Ferenczi. Wirelessly powered, fully internal optogenetics for brain, spinal and peripheral circuits in mice. *Nature Methods*, 2015.

[7] Logan Grosenick, James H Marshel, and Karl Deisseroth. Closed-Loop and Activity-Guided Optogenetic Control. Technical report.